

Crystallographic analysis of temperate ice on Rhonegletscher, Swiss Alps

Sebastian Hellmann^{1,2}, Johanna Kerch^{3,*}, Ilka Weikusat^{3,4}, Andreas Bauder¹, Melchior Grab^{1,2}, Guillaume Jouvét^{5,6}, Margit Schwikowski⁷, and Hansruedi Maurer²

¹Laboratory of Hydraulics, Hydrology and Glaciology (VAW), ETH Zurich, Zurich, Switzerland

²Institute of Geophysics, ETH Zurich, Zurich, Switzerland

³Alfred Wegener Institute Helmholtz Centre for Polar and Marine Research, Bremerhaven, Germany

⁴Department of Geosciences, Eberhard Karls University, Tuebingen, Germany

⁵Department of Geography, University of Zurich, Zurich, Switzerland

⁶Autonomous Systems Laboratory, ETH Zurich, Zurich, Switzerland

⁷Paul Scherrer Institute, Villigen, Switzerland

* now at: GZG Computational Geoscience, Georg-August University, Goettingen, Germany

Correspondence: Sebastian Hellmann (sebastian.hellmann@erdw.ethz.ch)

Abstract. The crystal orientation fabrics (COF) analysis provide information about the c-axis orientation of ice grains and the associated anisotropy and microstructural information about deformation and recrystallisation processes within the glacier. These information can be used to introduce modules that fully describe the microstructural anisotropy or at least direction-dependent enhancement factors for glacier modelling. The COF was studied at an ice core that was obtained from the temperate Rhonegletscher, located in the Central Swiss Alps. Seven samples, extracted at depths between 2 and 79 m, were analysed with an automatic fabric analyser. The COF analysis revealed conspicuous four-maxima patterns of the c-axis orientations at all depths. Additional data, such as microstructural images, produced during the ice sample preparation process, were considered to interpret these patterns. Furthermore, repeated high-precision Global Navigation Satellite System (GNSS) surveying allowed the local glacier flow direction to be determined. The relative movements of the individual surveying points indicated longitudinal compressive stresses parallel to the glacier flow. Finally, numerical modelling of the ice flow permitted estimation of the local stress distribution. An integrated analysis of all the data sets provided indications and suggestions for the development of the four-maxima patterns. The centroid of the four-maxima patterns of the individual core samples and the coinciding maximum eigenvector approximately align with the compressive stress directions obtained from numerical modelling with an exception for the deepest sample. The clustering of the c-axes in four maxima surrounding the predominant compressive stress direction is most likely the result of a fast migration recrystallisation. This interpretation is supported by air bubble analysis of Large-Area Scanning Microscope (LASM) images. Our results indicate that COF studies, which were so far predominantly performed at cold ice samples from the polar regions, can also provide valuable insights on the stress and strain [rate](#) distribution within temperate glaciers.

1 Introduction

20 Since the second half of the last century, ice cores have been regarded as extremely valuable archives for reconstructing the climate history of the past hundred-thousands of years (Robin et al., 1977; Petit et al., 1999; Thompson et al., 2002). For example, correlations between ice accumulation, isotopes and dust content have been established, but the deformation of ice layers complicates dating and interpretation of climate records (Jansen et al., 2016). Microstructural analyses have been used to overcome these issues (Faria et al., 2010). In addition, microstructural investigations have also been conducted to reconstruct

25 the ice flow of ice sheets in Greenland and Antarctica as well as in glaciated mountain areas (Russell-Head and Budd, 1979; Alley, 1992; Azuma, 1994). For those investigations, the focus has been on the crystallographic orientation of the ice grains. The stresses and [strains-strain rates](#) occurring within the ice mass not only cause glacier flow, but also induce the development of a characteristic COF and microstructural anisotropy (Gow and Williamson, 1976; Herron and Langway, 1982; Alley et al., 1995, 1997) and summarised in Faria et al. (2014a).

30 During the past decades, COF and texture have been investigated intensively on polar deep ice cores to understand the microstructure of polycrystalline ice in the context of its deformation history (Hooke, 1973; Gow and Williamson, 1976; Thorsteinsson et al., 1997; Patrick et al., 2003; Gow and Meese, 2007; Pettit et al., 2007; Montagnat et al., 2014; Pettit et al., 2011; Weikusat et al., 2017). A historical summary of these projects can be found in Faria et al. (2014a). For the selected ice core drilling spots on domes and ridges, vertical compression and horizontal extension within the ice mass have been found

35 to be the dominant driving stress for ice deformation. In contrast, for ice samples from temperate glaciers, the deformation is dominated by a series of interfering and changing compressional, extensional, and shear stress conditions along the valley. Together with a diagenesis, burial, basal sliding, and potentially partial melting these stress conditions results in a much more complex deformation history (Hambrey and Milnes, 1977). This requires more extensive analyses of COF.

The ice of temperate glaciers is comparable with a metamorphic rock close to its melting point (Hambrey and Milnes, 1977)

40 that has been exposed to a long series of deformation processes along the valley. This deformation is caused by various shear and compressional stresses that have been applied to the ice. These stress regimes produce heterogeneously distributed dislocations, which cause dynamic recrystallisation by rearrangement of these dislocations and by internal strain energy reduction. The resulting recrystallisation processes and the interplay between deformation and recrystallisation in the ice take place even faster as the temperature gets closer to the pressure melting point (Alley, 1988; Weikusat et al., 2009a). As a result, the adaption

45 of the ice crystal structure to new stress conditions is expected to be faster (e.g. Kamb, 1972; Duval, 1979). Additionally, the higher temperatures provide more thermal energy and allow a faster grain growth (Azuma et al., 2012), leading to an interplay between stress and temperature regime (Alley, 1988; Faria et al., 2014b). Therefore, large differences can be observed between cold and temperate ice. One of the most apparent differences is the grain size, which has been found to be a few centimetres in temperate ice (Rigsby, 1960), whereas samples from polar ice usually show grains with a diameter of a few millimetres, except

50 in the deepest parts, where temperatures rise close to the pressure melting point (e.g. Gow and Williamson, 1976; Thwaites et al., 1984; Kuiper et al., 2019).

First crystallographic investigations have been performed on temperate glaciers already in the 1950's to 1980's, including the

detailed investigations of Kamb (1959) and Rigsby (1960), and later extended by Budd (1972), Hambrey and Milnes (1977), Hooke and Hudleston (1978), and Hambrey et al. (1980). A potential problem of temperate glacier crystal analysis is the large grain size and thus limited amount of grains that can be analysed for each sample. This may be the reason, why a surprisingly low number of papers has been published on crystal structure of temperate glaciers (e.g. Tison and Hubbard, 2000) during the past years. Furthermore, the majority of the earlier studies mainly analysed samples from the uppermost few meters. To date, ice core drilling and preparation of thin sections is still a time-consuming process. Only a few discrete measurements are possible within a reasonable amount of time. Nonetheless, the technique for analysing COF has developed extensively, for example, by using image analysis software and powerful computing resources (Wilson et al., 2003; Peternell et al., 2009; Wilson and Peternell, 2011; Eichler, 2013).

In this study, we analyse ice core samples from a temperate alpine glacier. We describe and compare our findings with ~~studies from the last century~~ previous studies and provide a hypothesis for the resulting COF in terms of given stress and temperature conditions. We analyse the stress regime in the vicinity of the ice core, using additional borehole measurements and discuss recrystallisation processes and grain growth in temperate ice. For selected examples we take a closer look at the development of new ice crystals under the current stress regime of the glacier. The microstructural results of this study serve as a basis for geophysical experiments on ice core samples and they can also be compared with results from larger scale geophysical experiments.

2 Field Site and Data Acquisition

The field work was carried out on Rhonegletscher, located in the Central Swiss Alps (Fig. 1). This glacier currently covers an area of about 15.5 km² and is flowing in a southern direction from 3600 m a.s.l. down to 2200 m a.s.l. It is a medium-sized valley glacier, easily accessible, and therefore investigations had been carried out already in the last two centuries and continuously since 2006 (Bauder, 2018).

In August 2017, we drilled an ice core in the ablation area of the glacier (Fig. 1), approximately 500 m north of its current terminus. Here, the ice was flowing with an average surface velocity of 16.2 m a⁻¹ in the season 2017/18 according to GNSS measurements. This location was selected, because the glacier surface forms a relatively even plateau with only 5 m elevation change over a distance of 40 m and is free of crevasses. Further up-glacier there is a steep and crevassed area. An analysis of the bedrock with ground-penetrating radar measurements also confirmed a transition from a steep to a more flat zone of the valley (Church et al., 2018) at the ice core location.

As the ice is just at the pressure melting point, we used a thermal drilling technique (Schwikowski et al., 2014). Although hot-water drillings, performed in the vicinity of the ice core location, showed a mean ice thickness of 110 m, we stopped drilling at 80 m, when hitting some gravel. This gravel blocked the cutter head. We retrieved an 80 m long ice core, with a gap between 46 and 50 m due to technical issues.

Due to the thermal drilling technique, which did not apply a rotational force onto the ice core segments, an oriented retrieval of the segments was possible. A freshly drilled segment was manually connected to the previous one, which worked out well

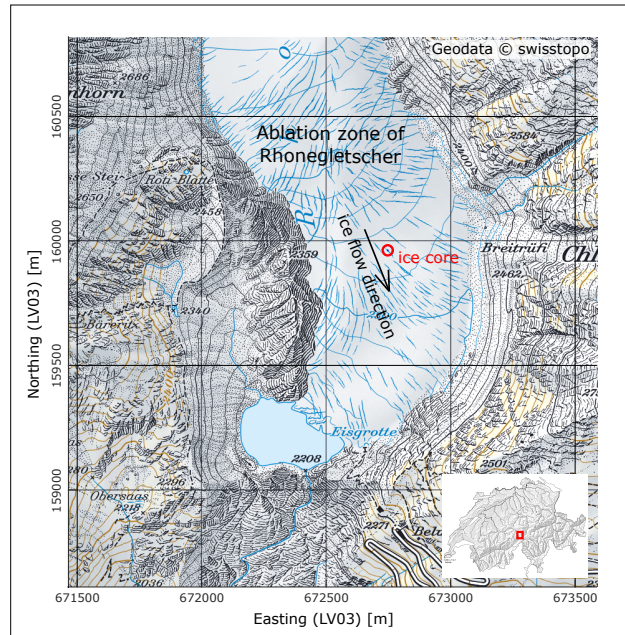


Figure 1. Rhonegletscher ablation area, ice core position indicated in red, ice flow direction at ice core location shown by black arrow. Map source: Swiss Federal Office of Topography.

for most of the segments. Additional measurements of the Earth’s magnetic field, while drilling, could be used in some cases to reconstruct the orientation within a range of $\pm 10^\circ$ when matching of neighbouring segments was not possible.

To complement the results of the ice core analysis, we made use of an array of hot-water-drilled boreholes surrounding the location of the ice core retrieval (Fig. 2). The locations of the borehole collars were surveyed repeatedly using high-precision GNSS measurements (Fig. 2a). The displacements of the borehole collars indicate a south-eastern flow direction with an azimuth of about $155^\circ \pm 10^\circ$. Besides determining the general flow direction from the absolute movements of the borehole collars, their relative displacements provided further insights. In We further derived the surface velocities at each borehole location (Fig. ??, the displacements of the individual borehole collars are plotted 2b). The south-eastern boreholes (BH04 to BH07) show significantly smaller displacements, compared with the boreholes located in the north-western part of the array (BH01 and BH10 to BH12). This indicates compression of the ice in this region, which is expected to lead to larger longitudinal strain rates (convention: compressional strain rates = negative values). We calculated the surface strain rate components $\dot{\epsilon}_{xx}$, $\dot{\epsilon}_{xy}$, and $\dot{\epsilon}_{yy}$ (Fig. 3) from these velocities. These strain rates and velocities serve as constraints for the ice flow modelling.

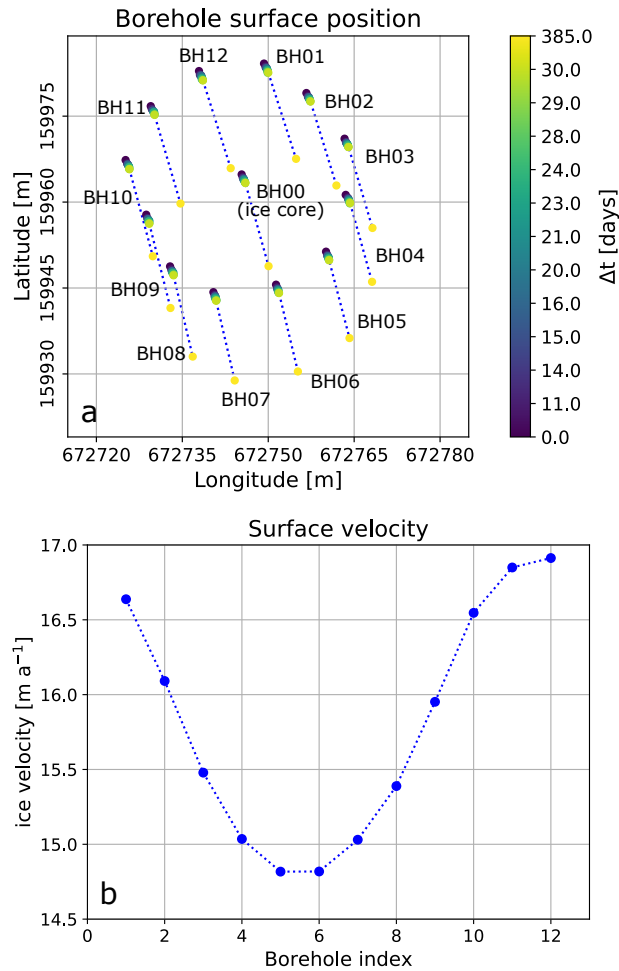


Figure 2. Analysis of ice flow direction and velocity for each borehole, (a) the displacement of the borehole surface points measured by GNSS is shown for each borehole with colours indicating the time since drilling, (b) the absolute surface velocity [m a⁻¹] in the vicinity of each borehole.

3 Ice flow modelling

100 To support these observations at the surface, the internal glacier dynamics was investigated by the means of a three-dimensional ice flow model that already existed from previous studies (Jouvet et al., 2009; Morgenthaler, 2019). An updated bedrock model and surface topographic information were used to determine the actual ice thickness of the glacier and to constrain the model. The bedrock model was obtained from GNSS measurements (Church et al., 2018) and from a Swiss-wide glacier inventory that is currently being updated (Farinotti et al., 2009; Grab et al., 2018). With the given information, we simulated the ice flow

105 of Rhonegletscher using the Elmer/Ice modelling code (Gagliardini et al., 2013), which solves the full Stokes equations based

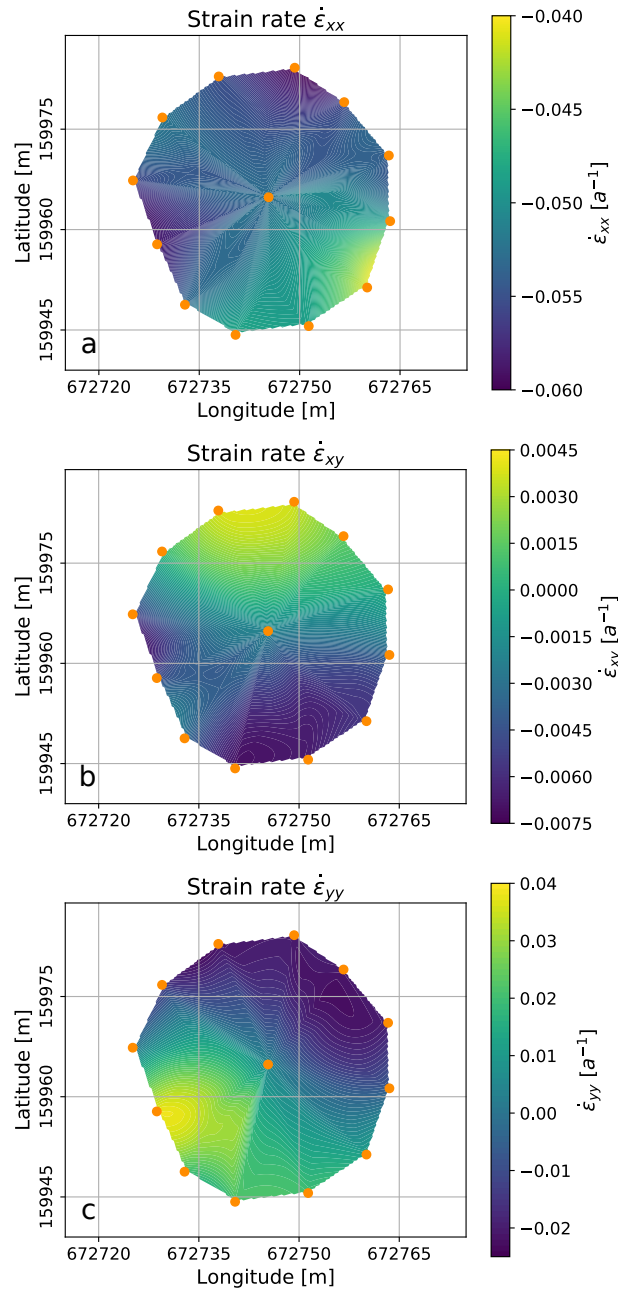


Figure 3. The ice flow analysis shows the absolute horizontal displacement of Strain rate components at the borehole collars surface derived from GNSS after 385 days for each borehole around the ice core hole flow velocity pattern shown in Fig. 2b, (borehole azimuthal direction relative to ice core hole) a) $\dot{\epsilon}_{xx}$, $N=0^\circ$ (b) $\dot{\epsilon}_{xy}$, (c) $\dot{\epsilon}_{yy}$; compressional strain rates = negative values, boreholes = orange dots.

on Glen's flow law (Glen, 1955) for the ice rheology, namely,

$$\dot{\epsilon}_{ij} = A(T) \tau^{n-1} \tau_{ij}, \quad (1)$$

where $\dot{\epsilon}_{ij}$ is the strain rate, τ_{ij} is the deviatoric stress, and τ is the second invariant of the deviatoric stress tensor. The creep exponent n was ~~chosen with~~ set to $n = 3$ as typical value for valley glaciers (Budd and Jacka, 1989). Basal sliding is modelled
110 by using Weertman's friction law as boundary condition at the ice-bedrock interface:

$$u_b = c \tau_b^{\frac{1}{m}} \quad (2)$$

where u_b is the norm of the basal velocity, τ_b is the basal shear stress, while ~~$m = 3$~~ and c are constant parameters. The main model parameters are the coefficient c and the rate factor A that control the amount of basal motion and internal deformation, respectively. As rate factor, we choose $A = 100 \text{ MPa}^{-3} \text{ a}^{-1}$, which was proved to correctly reproduce the velocities of
115 Aletschgletscher (Jouvet et al., 2011). The rate factor is close to the literature value for temperate ice ($76 \text{ MPa}^{-3} \text{ a}^{-1}$) (Cuffey and Paterson, 2010). As sliding coefficient, we used $c = 10 \text{ km MPa}^{-1}$, which was tuned such that the observed and modelled ice velocities match at the surface of the borehole. Additional bedrock-sliding velocity values with less than 5 m a^{-1} , estimated from borehole camera investigations (Gräff et al., 2017), supports our assumptions for this value. It is rather small compared to previous studies on Alpine glaciers (Jouvet and Funk, 2014; Compagno et al., 2019). Here, we ran the model in a stationary
120 fashion without time evolution. As model outputs, we obtained the velocity and stress field in three dimensions. For a sensitivity analysis, we also tested different rate factors and basal sliding coefficients. As the model still slightly overestimated the derived basal velocities, we also analysed the case without basal sliding ($c = 0 \text{ km MPa}^{-1}$). In this case, an extremely high rate factor $A = 200 \text{ MPa}^{-3} \text{ a}^{-1}$ was required to fit the measured velocities. Furthermore, the principal stress axes did not change significantly. These changes lead to a slightly enhanced longitudinal simple shear component and slightly weaker
125 longitudinal compressional component in the deepest parts of the ice. Therefore, we only considered $A = 100 \text{ MPa}^{-3} \text{ a}^{-1}$ and $c = 10 \text{ km MPa}^{-1}$ in the following analysis.

4 Crystal Orientation Fabric Analysis

For detailed structural investigations of the temperate glacier ice, we performed a COF analysis in the laboratories of the Alfred-Wegener-Institute Helmholtz Centre for Polar and Marine Research (AWI). We measured the orientation of the c-axes of the ice
130 grains. The c-axis is the symmetry axis perpendicular to the basal plane of a hexagonal crystal. Along the c-axis, the physical properties differ significantly from any direction parallel to the basal plane (the a-axes). ~~The~~ This results in an anisotropic viscous response of the glacier ice (Schulson and Duval, 2009, Chapt. 6). Furthermore, the elastic parameters of the ice, such as bulk or shear modulus, have enhanced values in the c-axis direction and the crystal is more resistant to deformation (Cuffey and Paterson, 2010, chapter 3). This ~~results in anisotropy effects, which leads to different velocities~~ anisotropy affects the
135 elastic properties leading to velocity changes for acoustic waves ~~travelling which travel~~ through the ice (e.g. Diez and Eisen, 2015).

From the ice core extracted from the central borehole BH00 (Fig. 2a), seven samples at depths of 2, 22, 33, 45, 52, 65 and 79 m were considered. Due to technical problems during the core retrieval, the azimuthal orientations of the samples at 2 and 45 m depth are subject to some uncertainties. Their azimuthal orientations were thus obtained from extrapolations from adjacent measurements.

Each of the seven samples consisted of an ice core segment of about 50 cm length. Up to four 11 cm long adjacent sub-samples (Fig. 4) were prepared from each of these segments. Each sub-sample was then further dissected into a horizontal and two vertical cuts. All three cuts are perpendicular to each other (Fig 4). This resulted in a horizontal circular slice and two vertical slices with SN- and EW-orientations from which thin sections were prepared. We measured between 8 and 12 thin sections per sample and 77 thin sections in total. This procedure enabled a more comprehensive analysis of the large crystals existing in temperate glacier ice (e.g. Kamb, 1959; Rigsby, 1960) and a tracing of fissures (also called fracture traces), for instance from potential meltwater intrusions. The dimensions of the pieces were 10×6 cm for the vertical sections and a diameter of ≈ 7 cm for the circular horizontal sections. The creation of sub-samples and choosing three different types of sections (horizontal, EW-vertical, SN-vertical) for every sub-sample resulted in a comprehensive analysis of at least 300 grains for each depth level. During the preparation of the ice thin sections, we also took large-area scanning microscope (LASM) images (Binder et al., 2013; Krischke et al., 2015) from the polished surface of the 1 cm thick ice samples. These images provide information on the grain boundary network, subgrain boundaries, as well as the air bubble distribution, since light from the active camera is backscattered to a great extent by the evenly polished ice surfaces. Uneven parts, such as air bubbles or grain boundaries, reduce the amount of backscattered light and appear darker in the image.

All sections were analysed using cross-polarised light (Wilson et al., 2003; Peternell et al., 2009). We used the automatic fabric analyser G50 from Russell-Head Instruments (Wilson et al., 2003) to measure the orientation of the c-axis on a predefined mesh grid with a pixel resolution of $20 \times 20 \mu\text{m}^2$. The orientation of the c-axis of an ice crystal is determined by two angles:

$$c(\vartheta, \varphi) = [\cos(\vartheta) \sin(\varphi), \sin(\vartheta) \sin(\varphi), \cos(\varphi)]. \quad (3)$$

The first angle defines the azimuth $\vartheta \in [0, 2\pi]$ of the c-axis in the horizontal plane. The second angle is the colatitude $\varphi \in [0, \frac{\pi}{2}]$ from vertical.

For the postprocessing of the obtained crystallographic data, we used the software *cAxes* (Eichler, 2013). *cAxes* analyses the misorientation angle between the determined c-axis orientations of neighbouring pixels and combines those with a misorientation $< 1^\circ$ to individual ice grains with a mean c-axis azimuth and colatitude per grain. The minimum grain size, calculated from the number of pixels multiplied by the pixel resolution, was set to 0.2 mm^2 (500 pixels). *cAxes* automatically rotated the vertical thin sections around the horizontal x-axis x' of the local measurement coordinate system (x', y', z') by 90° into the ice core system (x, y, z) with $z = \text{core's vertical axis}$ ($z = y'$ and $y = -z'$ pointing upwards (cf. Fig. 4)). Then, the thin sections were rotated around the vertical axis z towards the reference point that was engraved into the core segments (e.g. $\theta_{\text{EW}} = \theta_{\text{EW}} + 180^\circ$). For the horizontal sections, the two coordinate systems were already identical. In a final step, we used the magnetometer data to obtain the true azimuthal orientation for all thin sections of a sampling depth relative to geographic north. This ensures an identical coordinate reference frame for all types of thin sections along the whole ice core.

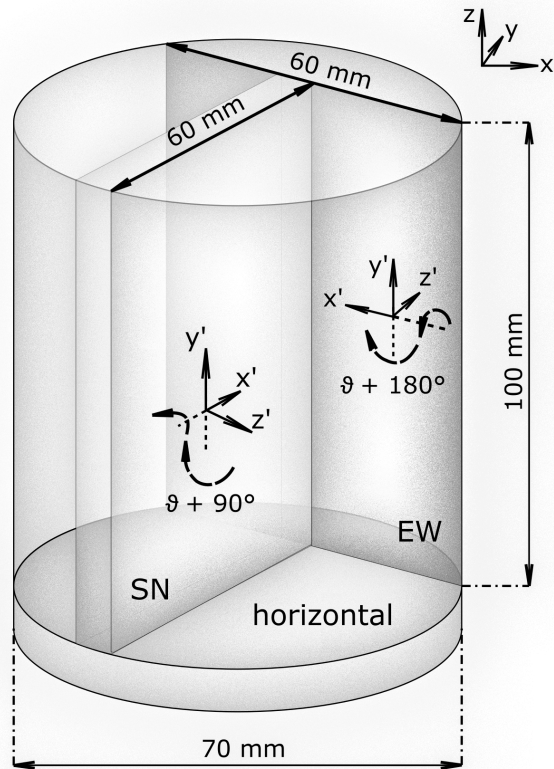


Figure 4. Cutting scheme for the ice core analysis. An 11 cm long piece of the ice core was cut in a horizontal ($d=7$ cm) and two vertical (east-west, south-north oriented, 10×6 cm) thin sections. Four thin sections of each type were analysed and combined per sampling depth.

Finally, we computed the eigenvalue distribution according to the procedure of Wallbrecher (1986). The three eigenvalues λ_i ($i=1, 2, 3$) follow the relations $\sum \lambda_i = 1$ and $0 \leq \lambda_3 \leq \lambda_2 \leq \lambda_1 \leq 1$. These eigenvalues represent the main axes of an ellipsoid ~~which~~ that presents the best fit for a given c-axis density distribution.

5 Results

175 Figure 5 shows the results of the COF analysis (left panels) and selected images of horizontal thin sections (right panels) for each depth level. The COF results are displayed in form of Schmidt equal-area stereo plots on the lower hemisphere (vertical core axis in centre). Results from all sub-samples and section orientations are combined. Each ice grain c-axis is represented by a dot. As shown by the images in the right panels of Fig. 5, the ice matrix is dominated by a few extremely large grains. Nevertheless, several hundred small grains appear along the grain boundaries or in specific patches. Especially the samples
 180 from 22 m and 45 m contain a large number of small grains. These grains form specific patterns looking like fracture traces,

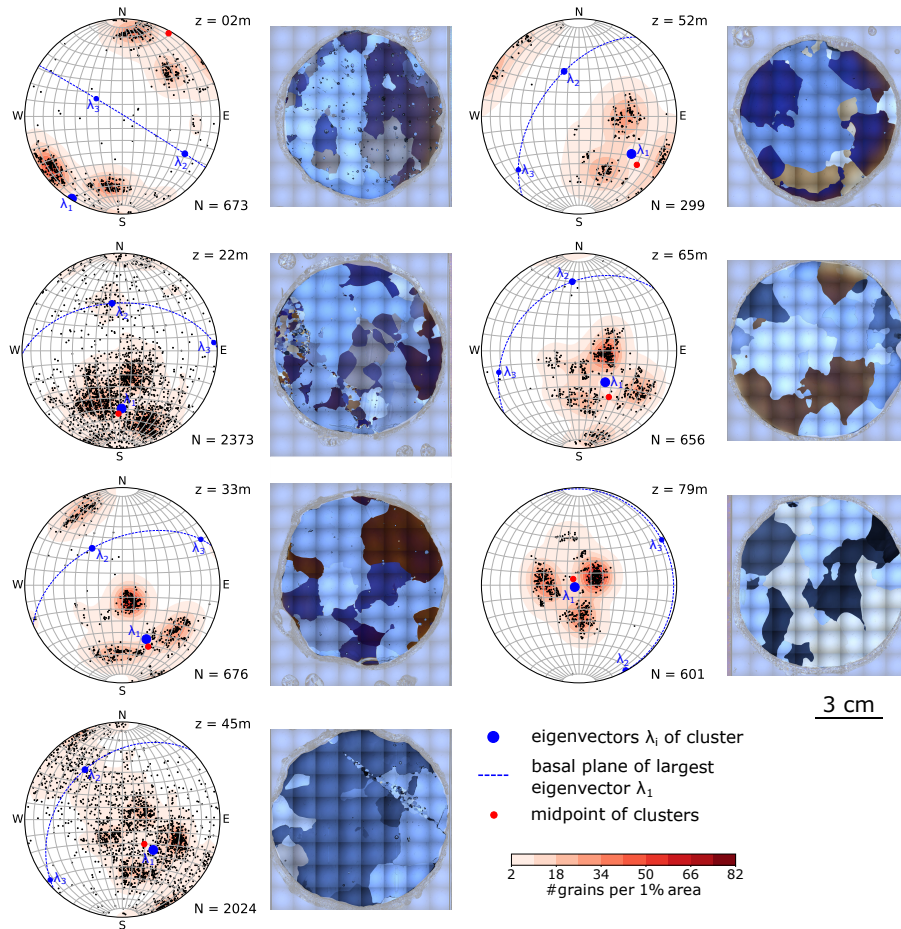


Figure 5. Left columns: Stereo plots (lower hemisphere Schmidt equal-area projection into the horizontal, i.e. long axis of core plots in the centre) with the c-axis distribution and associated horizontal thin sections, illustrating the typical grain size distribution, are shown for each sample. The total number of ice grains (N) is specified for each sample (consisting of at least 3 horizontal and 6 vertical thin sections, all rotated to horizontal view and common geographic coordinates). The sampling depth (z) is indicated at the upper right corner of the stereo plots. The colour code (smoothed Kamb's distribution (Vollmer, 1995)) emphasises the existing clusters of the c-axis distribution. The largest eigenvector for the determined distribution is depicted as blue dot and its normal plane is shown as dashed line. Right columns: example images of horizontal thin sections, recorded under cross-polarised light, pale edges around the actual samples are excluded from analysis.

which are traceable through several thin sections.

For better visualising the c-axis distributions, a smoothed colour density plot, calculated in accordance to Kamb's method (Vollmer, 1995), was superimposed on the stereo plots. These density plots only consider the number of grains within the area of the stereo plot, i.e. the size of the individual grains does not affect the colour code. All density plots indicate a multi-maxima pattern and the majority exhibits four maxima. The orientation of the patterns varies with depth, but the structure inside the

patterns is remarkably similar. The four maxima lie on a small circle girdle, which is characterised by an opening angle around a central vector, shown as a midpoint in the stereographic projection. Two maxima always lie on opposite sides of this midpoint and the other two on a line perpendicular to the first two clusters so that the azimuthal separation of the maxima is 90° . Deviations are observed at 45 m depth, where a fifth maximum at the horizontal margin appears, and at 79 m, where one of the four maxima is significantly weaker than the others. Depending on the number of grains per cluster the midpoint (red point in Fig. 85) differs from the actual centroid (blue dot λ_1 in Fig. 5) of the multi-maxima pattern. The opening angle between the midpoint and the individual maxima varies with $\pm 15^\circ$ around a mean of 30° (Table 1), but the mean value is constant over all depths.

The eigenvectors of the polycrystalline orientation tensor were calculated for each depth, and they are also shown in the stereo plots (blue dots in Fig. 5). For enhanced visibility, the plane normal to the eigenvector associated with the largest eigenvalue λ_1 is indicated with a dashed blue line. This eigenvector coincides with the centroid of the four-point-maxima. The other two eigenvalues are significantly lower than λ_1 ($0.56 \leq \lambda_1 \leq 0.7$) and usually in a range of $0.1 \leq \lambda_2 \leq 0.31$ and $0.09 \leq \lambda_3 \leq 0.13$, respectively.

With an exception for the uppermost depth at 2 m and the lowermost depth at 79 m, the azimuth of the maximum eigenvectors ($147^\circ \pm 31^\circ$) is aligned with the direction of the glacier's ice flow ($155^\circ \pm 10^\circ$, cf. Figs. 1, 2). With increasing depth, the maximum eigenvector has a decreasing colatitude, and at 79 m this eigenvector as well as the centroid of the cluster is almost vertically oriented.

Table 1. Angles between individual maxima and the centroid, i.e. the largest eigenvector, describing the relative geometry of the multi-maxima pattern and the absolute orientation (azimuth/colatitude) of the centroid.

depth [m]	relative angles within the cluster					absolute position of cluster	
	angles per maximum [$^\circ$]				mean angle [$^\circ$]	azimuth [$^\circ$]	colatitude [$^\circ$]
2	23.3	27.4	34.3	34.5	29.9 ± 4.7	211.5 (151.5)	88.6
22	23.5	25.3	34.5	35.2	29.6 ± 5.2	178	49.4
33	20.8	26.0	41.0	47.6	33.9 ± 10.9	156	50.6
45	26.9	29.2	30.7	33.2	30.0 ± 2.3	134.4	36.6
52	22.2	27.9	29.6	38.2	30.6 ± 5.7	125.6	55.7
65	20.6	22.5	34.7	37.6	28.9 ± 7.4	140.2	34.5
79	20.2	25.2	34.3	34.6	28.6 ± 6.1	246.6	3.9

For an enhanced and statistically significant data set, we combined the determined c-axis orientations, measured in up to twelve individual thin sections with three different orientations. However, the results from the different orientations of the sections (Fig. 4) may be inconsistent. Although the grains are not elongated in a certain direction (i.e. do not show a shape preferred orientation), some of them appear branched and interlocked (Fig. 5, right panels). Therefore, two-dimensional cuts through large, branched grains may let them appear as several individual grains within the same section. Kamb (1959) and Hooke

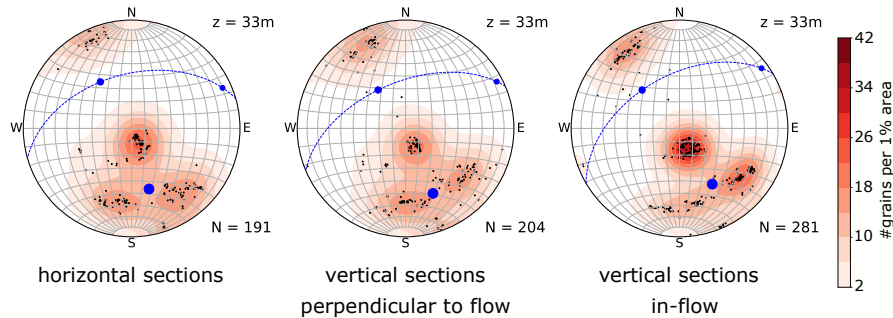


Figure 6. Stereo plots (lower hemisphere Schmidt equal-area projection) for the three types of sub-samples (horizontal, east-west, south-north, from left to right) with annotations as in Fig. 5.

(1969) have already discussed the statistical relevance of these branched grains. The sketch in Hooke and Hudleston (1980), Fig. 6, and more recently in Monz et al. (2020), Fig. 3, further illustrate this issue that could result in over-represented clusters in the superimposed stereo plots from the different sub-samples.

To check the consistency of the individual orientations, the c-axis distribution for each sub-section (horizontal, east-west and south-north) was analysed separately. Figure 6 shows the results for the sample at 33 m depth. All three sub-sections show a similar pattern. The individual maxima appear in all sections and are not a result of stitching differently orientated sections together. However, due to the afore-mentioned reasons, the actual grain size is difficult to determine. Individual analyses for the other depths showed similarly consistent results (not shown).

6 Interpretation

For our interpretation, we refer to the deviatoric stress tensor elements shown in Table. The absolute values are shown in Fig. ??7 ($\sigma_{xx}^{(d)}$ and $\sigma_{xy}^{(d)} \leq 0$). The x-component of the tensor elements is aligned with the longitudinal direction, i.e. the glacier flow, and the y-component is aligned with the transverse direction. Due to the flow evolution of the ice grains through the glacier, these grains are deformed under given stress conditions (Schulson and Duval, 2009, chapt. 5) (Schulson and Duval, 2009, Chapt. 5). As the glacier changes its flow direction, the ice crystals experience changing stress conditions leading to variations in the deformation regime. As a result, the c-axes of the ice grains are oriented in specific patterns, such as the multi-maxima structure that we observed in the current ice core. Stress and strain rate are directly linked via Glen's flow law and changing stress causes a change in deformation geometry. However, the particular orientation of ice grains is crucial as to whether the ice is easy to deform ("soft" direction) or whether it is further resistive ("hard" direction) against the currently applied deformation. For a detailed analysis of the current stress conditions at the ice core location, we use the ice flow model to derive the Cauchy stress, i.e. the deviatoric stress tensor. The deviatoric stress tensor $\sigma^{(d)}$ is derived from the normal stress tensor σ by subtracting the

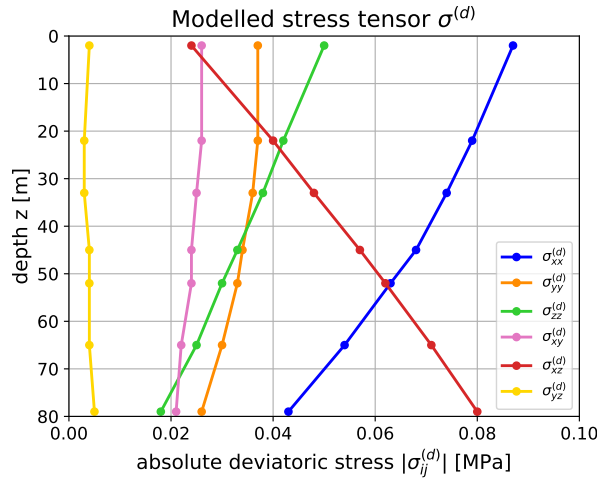


Figure 7. Stress-Absolute values of the deviatoric stress tensor elements obtained from ice flow modelling (x – longitudinal, y – transverse, z – vertical direction).

depth m $\sigma_{xx}^{(d)}$ $\sigma_{yy}^{(d)}$ $\sigma_{zz}^{(d)}$ $\sigma_{xy}^{(d)}$ $\sigma_{xz}^{(d)}$ $\sigma_{yz}^{(d)}$ 2 -0.087 0.037 0.050 -0.026 0.024 0.004 22 -0.079 0.037 0.042 -0.026 0.040 0.003 33 -0.074 0.036 0.038 -0.025 0.048 0.003 45 -0.068 0.034 0.033 -0.024 0.057 0.004 52 -0.063 0.033 0.030 -0.024 0.062 0.004 65 -0.054 0.030 0.025 -0.022 0.071 0.004 79 -0.043 0.026 0.018 -0.021 0.080 0.005

hydrostatic-isotropic pressure p from its main diagonal elements, i.e.

$$\sigma_{ij}^{(d)} = \sigma_{ij} - p\delta_{ij} \quad (4)$$

230 where $\delta_{ij} = 1$ for $i = j$, and $\delta_{ij} = 0$ otherwise. For the deformation of the ice grains only the deviatoric stress tensor is important.

The two most relevant components at the core location are the longitudinal compressional stress $\sigma_{xx}^{(d)}$ and the longitudinal shear stress $\sigma_{xz}^{(d)}$ (Table Fig. ??7). $\sigma_{xx}^{(d)}$ is the most dominant stress close to the surface. Its strength slightly decreases with depth. In addition, the shear stress $\sigma_{xz}^{(d)}$ governs the stress conditions in deeper parts as it increases with depth. The transverse components ($\sigma_{yy}^{(d)}$, $\sigma_{xy}^{(d)}$ and $\sigma_{yz}^{(d)}$) are more or less equal in all depths. We also calculate the strain rates $\dot{\epsilon}_{ij}$ from the stress tensor by using Glen's flow law, i.e. Eq. (1) (Table 2). Since the model does not consider anisotropy, the directions orientation dependent response of the anisotropic ice is not considered. For typical fabrics (e.g. single maximum, girdle fabric), enhancement factors could be introduced (e.g. Thorsteinsson, 2001; Pettit et al., 2007; Ma et al., 2010) to overcome this issue. Beyond, anisotropic flow laws (e.g. Gillet-Chaulet et al., 2005) can be employed to consider more complex fabrics such as

240 the multi-maxima pattern. Furthermore, in isotropic models, stress and strain rate are connected with a scalar value and the principal axes of stress and strain rate tensors are parallel. This is-These are a crucial limitation to be considered in the following interpretation. Especially for shear stress, the model-derived and the actual strain rate directions may differ significantly. In addition, the quantitative numbers deviate from isotropic ice as the aforementioned basal sliding affects the strain rates that an

Table 2. Strain rates derived from ~~borehole measurements and from~~ ice flow modelling (x – longitudinal, y – transverse, z – vertical direction).

depth [m]	$\dot{\epsilon}_{xx}$ [a ⁻¹]	$\dot{\epsilon}_{yy}$ [a ⁻¹]	$\dot{\epsilon}_{zz}$ [a ⁻¹]	$\dot{\epsilon}_{xy}$ [a ⁻¹]	$\dot{\epsilon}_{xz}$ [a ⁻¹]	$\dot{\epsilon}_{yz}$ [a ⁻¹]
2	-0.061	0.026	0.035	-0.018	0.017	0.002
22	-0.056	0.026	0.030	-0.018	0.028	0.002
33	-0.053	0.026	0.027	-0.018	0.034	0.002
45	-0.049	0.025	0.024	-0.018	0.041	0.003
52	-0.047	0.024	0.023	-0.017	0.046	0.003
65	-0.042	0.023	0.019	-0.017	0.055	0.003
79	-0.036	0.021	0.014	-0.017	0.065	0.004

ice grain experiences. ~~For more typical fabrics (e.g. single maximum, girdle fabric), enhancement factors could be introduced~~
245 ~~(e.g. Thorsteinsson, 2001; Pettit et al., 2007), but this is too complex for the multi-maxima patterns.~~ However, we regard the
modelling output as auxiliary values for our interpretation.

In the following, we provide an interpretation of three significant features presented in Fig. 5, namely

- the azimuthal orientation of the c-axes distributions as represented by the maximum eigenvectors of the stress tensors,
- the decrease of the maximum eigenvector colatitudes with increasing depths (viz. this eigenvector becomes more verti-
250 cal), and
- the existence of multi-maxima patterns in the c-axis distributions.

To support the interpretation, the stereo plots in Fig. 5 are shown again in Fig. 8 with adjustments as a result of the following
interpretation. Here, only the colour-coded c-axis density distributions are plotted, superimposed by additional information
obtained from accompanying analyses.

255 6.1 Azimuthal orientation

Results from all depth levels, with the exception for 2 m (Fig. 5), show in general a mean c-axis orientation (Table 1) approxi-
mately parallel to the main glacier flow direction that was obtained from the displacements of the surrounding boreholes (Fig. 2,
 $\approx 155^\circ$). The largest eigenvector λ_1 always lies in a vertical plane that is aligned ($\pm 20^\circ$) with the glacier flow direction. This
flow kinematics, depicted by the principal stress axis (~~Fig~~Figs. 5 and 8) is associated with the alignment of the centroid of the
260 c-axes. As this flow direction changes, the COF have most likely developed ~~in the last four decades~~ since the glacier flows in
the direction observed at our drill location. Although the centroid in 79 m is vertically oriented, the characteristic “diamond
shape” of the multi-maxima pattern is still joining the vertical plane of the glacier flow direction (the verticality of the pattern
is discussed below).

The observed azimuthal alignment of the COF with the glacier flow (with some limitations for 79 m) is in accordance with

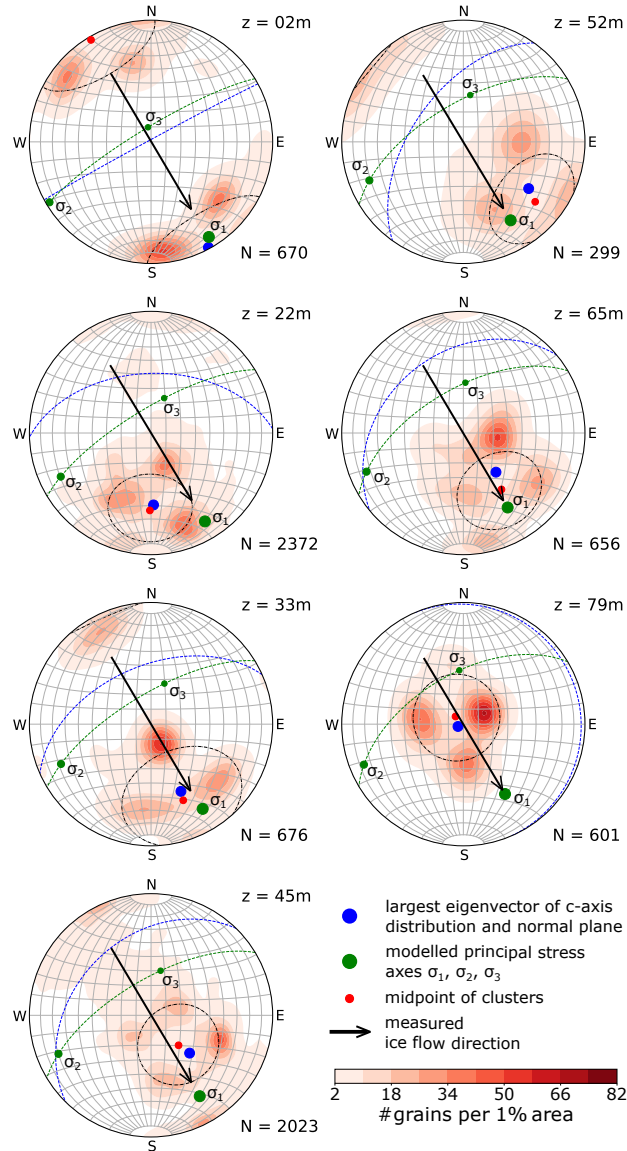


Figure 8. Stereo plots (lower hemisphere Schmidt equal-area projection) with the colour coded (same as Fig. 5) c-axis distribution for each sample are shown. Note: The azimuth for $z=2\text{ m}$ is corrected by -60° (see text for discussion). The total number of ice grains is specified for each sample. The black dashed line shows the mean opening angle for the cone of maxima around the centroid depicted as red dot. The calculated largest eigenvector for the c-axis distribution is shown as blue dot (its normal plane as dashed blue line) and the calculated largest compressional principal stress axis from the ice flow model is represented by a green dot (its normal plane as dashed green line).

265 results from laboratory experiments in a number of previous studies (e.g Kamb, 1972; Duval, 1981; Budd and Jacka, 1989) and comparable with some parts of the Cape Folger ice core (Thwaites et al., 1984).

The uppermost sample (2 m) does not fit into this interpretation. Although the magnetometer data are consistent, the core break between two segments at 10 m was unclear and we cannot fully exclude a misorientation between the segments in 2 and 22 m. As shown in Fig. 8 an azimuthal correction of -60° would lead to a perfect alignment of this sample with all other observations and the modelling results for the particular location. Therefore, we assume a misorientation of the core segments.

6.2 Colatitude variations

In the following, we consider the variations of the colatitude of the largest eigenvector λ_1 (Fig. 8, blue dot). There is a decrease of the colatitude from 89° to 4° with increasing depth (Table 1). Considering the deformation mechanisms, mainly dislocation creep, this is the result of the stress and strain rate distribution (Tables Fig. 7 and Table ?? and 2) in the glacier. The ice crystal c-axes in our samples generally orient themselves parallel to the ice flow, which coincides with the modelled maximum compressional principal stress direction (σ_1 in Fig. 8). As indicated by the relative movements of the surrounding boreholes (Fig Figs. ??2 and 3), we indeed observe a compression at the glacier surface. In accordance with borehole inclination measurements, the flow-parallel compression also occurs at greater depths but slightly decreases. In contrast, with increasing depth, the shear stress significantly increases. Especially in the deepest parts of the ice core, the longitudinal shear component $\sigma_{xz}^{(d)}$ governs the stress state, which is also confirmed by the inclinometer measurements. This increasing shear deformation of the ice lets the colatitude angle decrease with increasing depths, and explains, at least qualitatively, the observations in Fig. 8.

The principal stresses ($\sigma_1, \sigma_2, \sigma_3$), derived from the ice flow model, were added to Fig. 8 (green dots) for comparison. Although not matching perfectly, the colatitudinal angles of the largest eigenvector λ_1 and the dominant principal stress σ_1 are similar within $\pm 26^\circ$ with an exception for the deepest sample. The discrepancy especially for the deepest sample is considered as evidence that the c-axis distribution is governed by strain and not stress in the last consequence (Budd et al., 2013; Faria et al., 2014b; Weikusat et al., 2017). In the presence of simple shear, the direction of the principal stress axis and principal strain rate axis are not aligned (non-coaxial relation) Cuffey and Paterson (2010, Chapt. 3). This implies that the COF for the deepest sample is dominated by the shear component, which approaches simple shear. According to our strain rate components (Table 2) such an implication is justified. The modelled shear strain rate is twice as large as any other component and causes the most significant effect in the borehole measurements after a short time period.

6.3 Multi-maxima c-axes distribution

If the c-axis orientations would be governed solely by the orientation of the major principal stress and strain rate direction (σ_1) (mainly a result of compressional and simple shear stress), we would rather expect a single maximum in the stereo plots as in deeper parts of other ice cores (Faria et al., 2014a). As observed in Figs. 5 and 8, there is no single maximum. Instead, the individual c-axes in our samples deviate on average about 30° from the principal stress or strain rate (for 79 m) direction (indicated by black small circle girdles in Fig. 8) and group in several maxima.

The most likely reason for this observation involves recrystallisation processes. For our interpretation we follow the approach of

Table 3. Grain size distribution (median, mean, and maximum grain sizes [mm²], minimum grain size is 0.2 mm² and defined as threshold during processing) and number of grains within defined grain size classes [mm²].

depth [m]	number of grains	median	mean	max	number of grains per class					
					<1	1-5	5-20	20-100	100-500	>500
2	673	5.30	77.06	1826.71	211	123	102	135	76	26
22	2373	0.79	19.04	1551.97	1340	584	192	165	69	23
33	676	4.41	85.97	3994.17	202	146	110	106	83	29
45	2024	0.88	29.89	3249.29	1078	522	173	133	91	27
52	299	14.67	121.42	1986.70	52	56	49	66	55	21
65	656	6.01	95.02	3752.65	195	119	123	112	67	40
79	601	6.81	96.79	3236.18	141	134	109	111	79	27

Faria et al. (2014b), who distinguish between three In general, two types of recrystallisation :rotational have been considered, namely rotation recrystallisation (RRX) ,and two very similar but significantly different types of and migration recrystallisation (Alley et al., 1995). RRX (described in detail in Alley (1988)) counteracts against the dynamic grain growth (Weikusat et al., 2011b) . According to Faria et al. (2014b), migration recrystallisation, also called strain-induced boundary migration (SIBM)-, needs to be subdivided into two types, namely SIBM-O and SIBM-N. In both cases, grains with less dislocations grow at the cost of grains with a large amount of dislocations. The first type assumes that under given strain rate conditions, already existing (i.e. old), suitably oriented grains grow at the cost of less suitably oriented grains (called SIBM-O). The second type is very similar, but with a relevant difference: when the grain grows parts at the boundaries like bulges can be nuclei for new smaller grains (therefore called SIBM-N, see an exemplary process described by Steinbach et al. (2017) with a very similar orientation like their parent grain). These new grains are considered as strain-free grains and have an impact on the grain size. Both mechanisms are driven by reducing the thermodynamic energy of the whole system and grains with heterogeneously distributed dislocations are absorbed (Weikusat et al., 2009b, Fig. 8).

In our data set we observe a variety of different grain sizes. Table 3 summarises the grain size distribution in our ice core samples. As mentioned earlier, the two-dimensional cuts through the ice core samples may lead to a misinterpretation of the grain sizes as large interlocked grains can appear as several small grains. However, it can be expected that not all small grains are cut branches of large grains. We also analysed the COF for six different grain size classes individually. The data are shown in Fig. 9 for one sample (other samples in the supplement). The multi-maxima pattern is persistent in all grain size classes.

Based on these findings, we postulate that this pattern is a result of SIBM-N in combination with the described longitudinal compressional and shear stress.

However, our data set cannot conclusively explain the very regular distribution of c-axes, i.e. the "diamond shape", within the multi-maxima pattern.

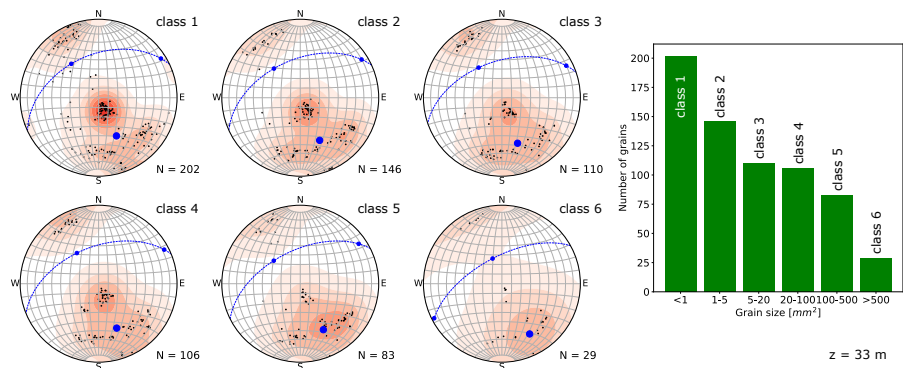


Figure 9. Stereo plots (lower hemisphere Schmidt equal-area projection) with the colour coded (same as Fig. 5). Each plot represents a grain size class as indicated at the upper right corner. The number of grains per class is specified for each plot. The calculated largest eigenvector for the c-axis distribution is shown as blue dot (its normal plane as dashed blue line). Right column: histogram showing the number of grains per class.

7 Discussion

320 The literature on COF field studies is not conclusive concerning the existence of multi-maxima fabrics. They were observed in early studies on temperate glaciers (e.g., Rigsby, 1951; Kamb, 1959; Rigsby, 1960) for the first time. In the 1970's to 1980's, they have been found in ice caps with ice temperatures above -10°C (Hooke and Hudleston, 1980), and also in the bottom ice of Byrd Station and Cape Folger in Antarctica (Gow and Williamson, 1976; Thwaites et al., 1984). At that time, the estimation of c-axis distributions was more subjective and could not benefit from modern equipment. The orientation of crystals was
 325 determined manually on a Rigsby-stage by turning and tilting the ice samples between polarised plates. Thus, only a limited number of grains (up to 100) and usually the largest grains were analysed. Therefore, the “diamond shape” pattern was often debated to be a statistical effect.

Interestingly, in more recent studies on other temperate glaciers multi-maxima fabrics in combination with a large grain size were only observed in the deepest parts of the ice cores drilled in the ablation zone (e.g. Tison and Hubbard, 2000). The conditions for a “diamond shape” pattern seem to be suitable in large glaciers like the Rhonegletscher with its high temperatures and large ice flow velocities compared to other valley glaciers. In polar ice cores, a multi-maxima fabrics has been observed only
 330 in the deepest parts of some Antarctic and Greenlandic cores (Gow and Williamson, 1976; Thwaites et al., 1984; Montagnat et al., 2014). There, the temperature conditions are as high as in temperate glaciers like the Rhonegletscher.

Laboratory experiments, performed on artificial ice under high temperatures ($> -2^{\circ}\text{C}$), provide evidence for two features
 335 we observe. Maohuan et al. (1985) created multi-maxima fabrics with combined shear and compressional stresses in their torsion-compression-experiments. The pattern clustered around the maximum principal stress direction. In addition, Jacka and Maccagnan (1984) analysed the opening angle of small circle girdles formed under compressional stress. The ranges for the opening angles are identical with our observations. For such opening angles between compressional direction and the

c-axis direction, the compressive strength applied onto the ice crystal is minimised (Schulson and Duval, 2009, chapter 11)

340 (Schulson and Duval, 2009, Chapt. 11).

As a result of these laboratory experiments and field measurements, we conclude that ~~the these temperate~~ conditions in Rhone-
gletscher ~~with high temperatures are an are a~~ prerequisite for the development of multi-maxima patterns. ~~Thus, , but~~ a multi-
maxima pattern is not necessarily found in all temperate glaciers.

Recrystallisation has regularly been observed in a variety of ice cores (Alley, 1988; Duval and Castelnau, 1995; Weikusat
345 et al., 2009b; Schulson and Duval, 2009; Cuffey and Paterson, 2010; Faria et al., 2014b). ~~In most of these papers, two types of
recrystallisation have been considered, namely rotation recrystallisation (RRX)~~ Recrystallisation has usually been divided into
two types – rotation and migration recrystallisation (Alley et al., 1995). ~~RRX (described in detail in Alley (1988)) counteracts
against the dynamic grain growth (Weikusat et al., 2011b). According~~ However, according to Faria et al. (2014b), migration re-
crystallisation, also called strain-induced boundary migration (SIBM), needs to be subdivided into two types ~~, namely~~ (SIBM-O
350 and SIBM-N). ~~In both cases, grains with less dislocations grow at the cost of grains with a large amount of dislocations. For
SIBM-O an already existing grain grows further and further. In case of SIBM-N new small and strain-free grains nucleate
from the original parent grain (often along the grain boundaries) and start to grow on their own. Both mechanisms are driven by
reducing the thermodynamic energy of the whole system and grains with heterogeneously distributed dislocations are absorbed
(Weikusat et al., 2009b, Fig. 8) However, these~~ These two mechanisms lead to different COF. If SIBM-O is the dominating pro-
355 cess, a single maximum consisting of a few very large grains is expected to develop. For SIBM-N we regularly generate new
grains with a similar orientation like the parent grain and concurrent maxima are likely to develop. This can lead to the ob-
served multi-maxima fabric. Evidence for a dominating grain boundary migration with nucleation (SIBM-N) can be observed
in LASM scans (Fig. 10). Firstly, the air bubbles are trapped within grains with a diameter of centimetres. Secondly, the grain
boundaries of neighbouring grains bulge and smaller grains develop either as “island grains” or as clusters along the bound-
360 aries of the large grains (blue, red and yellow circles in Fig. 10). The trapped air bubbles and newly developing grains provide
evidence that SIBM-N is the dominating process in these samples of temperate ice.

The recrystallisation does not conclusively provide arguments for the regular “diamond shape” within the multi-maxima pat-
tern. One potential mechanism to be considered are localisation effects. In this theory, the polycrystalline system distributes
the impact of the different strain along localisation bands, especially in presence of additional aggregates such as air bubbles
365 (Steinbach et al., 2016). This may lead to a highly variable rate of fabric change. A detailed investigation of localisation bands
is rather difficult in presence of grain boundary migration (i.e. SIBM-O and SIBM-N) as recrystallisation restores the crystal
shape and removes the typical shear bands (Llorens et al., 2016). Llorens et al. (2017) investigated the COF for simple shear
experiments by considering localisation bands and dynamic recrystallisation (rotational recrystallisation and grain boundary
migration, but without nucleation). These strain-induced localisation effects might be worth to be considered for explaining
370 multi-maxima patterns.

Further alternative explanations can and should be considered: Kamb (1959) calculated the preferred maximum positions of a
“diamond shape” pattern with considerations of single crystal compliance constants under recrystallisation. This explanation
could add missing details to our interpretation and describe the regularity in the “diamond shape” pattern. Matsuda and Waka-

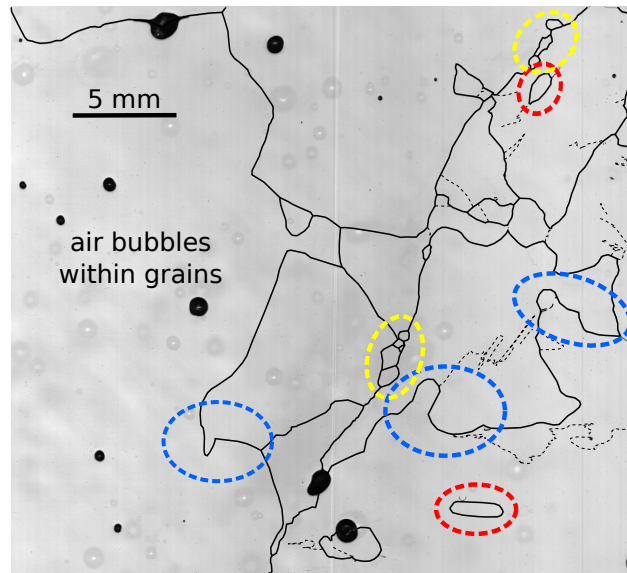


Figure 10. Example of a LASM image indicating several processes in the temperate ice: black areas are air bubbles, black lines represent the grain boundaries, and black dashed lines indicate subgrain boundaries. Air bubbles can be found completely trapped within individual large ice grains indicating migration recrystallisation. Bulging of grain boundaries (blue circles), the development of island grains (red circles) and small grains along the boundaries of large grains (yellow circle) provide evidence for a dominating SIBM-N-type recrystallisation.

hama (1978) suggest twinning effects that may occur when c-axes develop under recrystallisation. Potentially, these effects
 375 may lead to a clustering of the c-axes and would even better explain the regular shape of the COF. This theory is supported by
 the fact that the opening angles of two opposing clusters are generally similar, whereas the angles compared to the other two
 maxima can vary within 15-20° and therefore called “diamond shape” fabrics. Apart from that, it is hard to find any studies
 about observations on twinning as result of ice deformation in glaciers and Faria et al. (2014b) summarised that mechanical
 twinning has not been observed in glacier ice. To investigate this further, we would need to measure the orientation of the ice
 380 crystals a-axes (in addition to the c-axes), for an enhanced image about the crystal orientation in three dimensions (Weikusat
 et al., 2011a; Journaux et al., 2019; Monz et al., 2020).

8 Conclusions

COF analyses of an ice core, extracted from a temperate alpine glacier, showed conspicuous multi-maxima patterns of the
 c-axes. This was observed at different depth levels. The azimuth and colatitude of the centroid of these multi-maxima patterns
 385 are well-aligned with the main principal stress direction. Close to the surface, compressional longitudinal stress conditions
 lead to a horizontal orientation aligned with the glacier flow. In deeper parts, the dominating longitudinal shear stress causes a
 vertical COF. The mean basal plane is aligned with the shear plane.

Strain-induced boundary migration with nucleation of new grains (SIBM-N) seems to be the dominating recrystallisation

process under the given high temperatures and strain rates. This provides an explanation for the large and branched grains
390 accompanied by smaller grains with similar orientation and thus a clustering in several maxima. However, the observations
cannot conclusively provide an answer for the ~~characteristic~~-very regular “diamond shape” pattern.

To the best of our knowledge, this is the first comprehensive COF analysis of an ice core from a temperate alpine glacier that
links the COF with the glacier flow. The results are consistent with supporting measurements and modelling results. These
consistencies are encouraging, and will hopefully motivate similar studies on other temperate glaciers.

395 *Data availability.* The ice fabric data are published in the open-access database PANGAEA® (Hellmann et al., 2018) and are available upon
request. <https://doi.pangaea.de/10.1594/PANGAEA.888518>

Appendix A

Author contributions. This study was initiated and supervised by HM, AB, IW and MS. The field and laboratory data were collected by MS,
SH, MG, AB and JK and analysed by SH with support from JK and under supervision of IW and MS. Data processing and calculations were
400 made and interpreted by SH and discussed with JK, IW, and MG. The ice flow was modelled by GJ with input data from MG. The paper was
written by SH with comments and suggestions for improvements from all co-authors.

Competing interests. The authors declare that they have no conflict of interest.

Acknowledgements. This project is funded by the Swiss National Science Foundation under the SNF ~~Grant~~-Grants 200021_169329/~~1-1~~
and 200021_169329/2. Data acquisition has been provided by the Paul-Scherrer Institute, Villingen, the Alfred Wegener Institute Helmholtz
405 Centre for Polar and Marine Research (AWI), Bremerhaven and the Laboratory of Hydraulics, Hydrology and Glaciology (VAW) of ETH
Zurich. We especially thank J. Eichler, T. Gerber, T. Jenk, and D. Stampfli for their extensive technical and logistical support during ice
core drilling and processing. Valuable discussions with the Structural Glaciology group at University of Tuebingen helped to improve the
paper. We would like to thank the editor, Olivier Gagliardini, and the two reviewers, Erin Pettit and Peter Hudleston, for their constructive
comments, which greatly improved the quality of the manuscript.

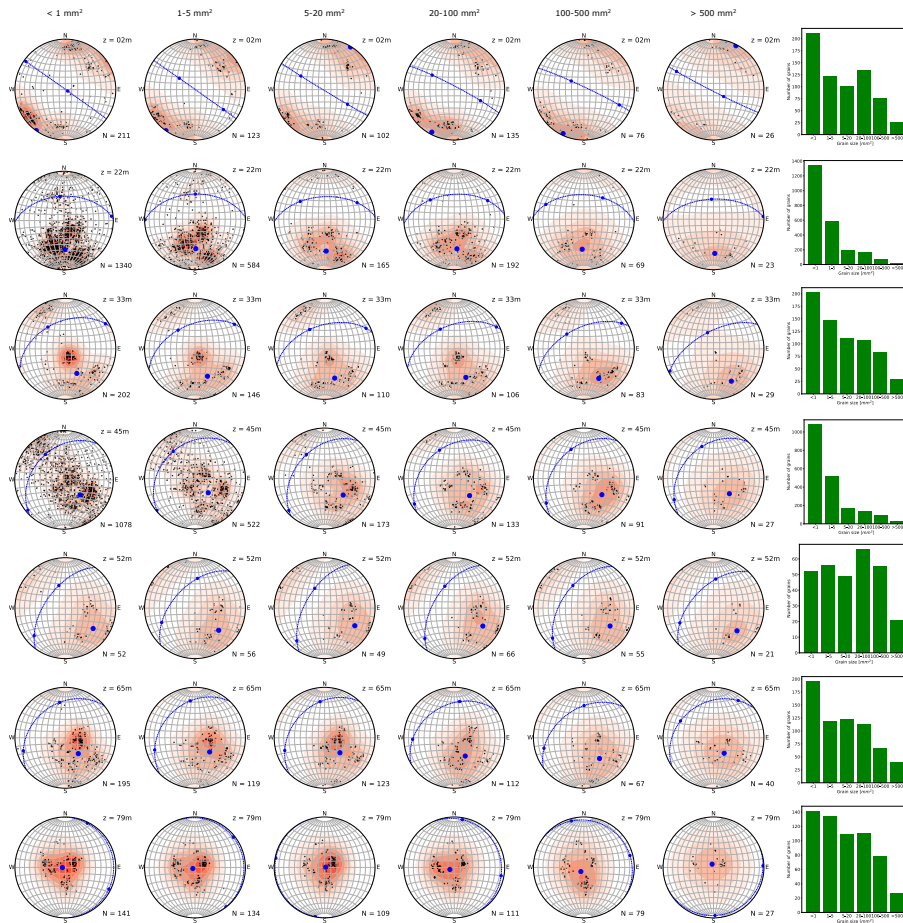


Figure A1. Stereo plots (lower hemisphere Schmidt equal-area projection) with the colour coded (same as Fig. 5). Each column represents a grain size class as indicated at the top. Each line represents one of the 7 samples of Fig. 5. The number of grains per class is specified for each plot. The calculated largest eigenvector for the c-axis distribution is shown as blue dot (its normal plane as dashed blue line). Last column: histograms showing the number of grains per class for each sample.

410 References

- Alley, R. B.: Fabrics in Polar Ice Sheets: Development and Prediction, *Science*, 240, 493–495, 1988.
- Alley, R. B.: Flow-Law Hypotheses for Ice-Sheet Modeling, *Journal of Glaciology*, 38, 245–256, 1992.
- Alley, R. B., Gow, A. J., and Meese, D. A.: Mapping C-Axis Fabrics to Study Physical Processes in Ice, *Journal of Glaciology*, 41, 197–203, 1995.
- 415 Alley, R. B., Gow, A. J., Meese, D. A., Fitzpatrick, J. J., Waddington, E. D., and Bolzan, J. F.: Grain-Scale Processes, Folding, and Stratigraphic Disturbance in the GISP2 Ice Core, *Journal of Geophysical Research: Oceans*, 102, 26 819–26 830, <https://doi.org/10.1029/96JC03836>, 1997.
- Azuma, N.: A Flow Law for Anisotropic Ice and Its Application to Ice Sheets, *Earth and Planetary Science Letters*, 128, 601–614, [https://doi.org/10.1016/0012-821X\(94\)90173-2](https://doi.org/10.1016/0012-821X(94)90173-2), 1994.
- 420 Azuma, N., Miyakoshi, T., Yokoyama, S., and Takata, M.: Impeding Effect of Air Bubbles on Normal Grain Growth of Ice, *Journal of Structural Geology*, 42, 184–193, <https://doi.org/10.1016/j.jsg.2012.05.005>, 2012.
- Bauder, A., ed.: The Swiss Glaciers 2015/16 and 2016/17, vol. 137/138 of *Glaciological Report*, Cryospheric Commission (EKK) of the Swiss Academy of Sciences (SCNAT), https://doi.org/10.18752/glrep_137-138, 2018.
- Binder, T., Garbe, C. S., Wagenbach, D., Freitag, J., and Kipfstuhl, S.: Extraction and Parametrization of Grain Boundary Networks in Glacier
- 425 Ice, Using a Dedicated Method of Automatic Image Analysis, *Journal of Microscopy*, 250, 130–141, <https://doi.org/10.1111/jmi.12029>, 2013.
- Budd, W. F.: The Development of Crystal Orientation Fabrics in Moving Ice, *Z. Gletscherkd. Glazialgeol*, 8, 65–105, 1972.
- Budd, W. F. and Jacka, T. H.: A Review of Ice Rheology for Ice Sheet Modelling, *Cold Regions Science and Technology*, 16, 107–144, [https://doi.org/10.1016/0165-232X\(89\)90014-1](https://doi.org/10.1016/0165-232X(89)90014-1), 1989.
- 430 Budd, W. F., Warner, R. C., Jacka, T. H., Li, J., and Treverrow, A.: Ice Flow Relations for Stress and Strain-Rate Components from Combined Shear and Compression Laboratory Experiments, *Journal of Glaciology*, 59, 374–392, <https://doi.org/10.3189/2013JoG12J106>, 2013.
- Church, G. J., Bauder, A., Grab, M., Hellmann, S., and Maurer, H.: High-Resolution Helicopter-Borne Ground Penetrating Radar Survey to Determine Glacier Base Topography and the Outlook of a Proglacial Lake, in: 2018 17th International Conference on Ground Penetrating Radar (GPR), pp. 1–4, IEEE, Rapperswil, <https://doi.org/10.1109/ICGPR.2018.8441598>, 2018.
- 435 Compagno, L., Jouvét, G., Bauder, A., Funk, M., Church, G., Leinss, S., and Lüthi, M. P.: Modeling the Re-Appearance of a Crashed Airplane on Gauligletscher, Switzerland, *Frontiers in Earth Science*, 7, <https://doi.org/10.3389/feart.2019.00170>, 2019.
- Cuffey, K. M. and Paterson, W. S. B.: *The Physics of Glaciers*, Elsevier, Amsterdam, fourth edn., 2010.
- Diez, A. and Eisen, O.: Seismic Wave Propagation in Anisotropic Ice – Part 1: Elasticity Tensor and Derived Quantities from Ice-Core Properties, *The Cryosphere*, 9, 367–384, <https://doi.org/10.5194/tc-9-367-2015>, 2015.
- 440 Duval, P.: Creep and Recrystallization of Polycrystalline Ice, *Bulletin de Minéralogie*, 102, 80–85, <https://doi.org/10.3406/bulmi.1979.7258>, 1979.
- Duval, P.: Creep and Fabrics of Polycrystalline Ice Under Shear and Compression, *Journal of Glaciology*, 27, 129–140, <https://doi.org/10.3189/S002214300001128X>, 1981.
- Duval, P. and Castelnau, O.: Dynamic Recrystallization of Ice in Polar Ice Sheets, *Le Journal de Physique IV*, 5, C3–197, 1995.
- 445 Eichler, J.: C-Axis Analysis of the NEEM Ice Core—An Approach Based on Digital Image Processing, Diploma Thesis, Freie Universität Berlin, 2013.

- Faria, S. H., Freitag, J., and Kipfstuhl, S.: Polar Ice Structure and the Integrity of Ice-Core Paleoclimate Records, *Quaternary Science Reviews*, 29, 338–351, <https://doi.org/10.1016/j.quascirev.2009.10.016>, 2010.
- Faria, S. H., Weikusat, I., and Azuma, N.: The Microstructure of Polar Ice. Part I: Highlights from Ice Core Research, *Journal of Structural Geology*, 61, 2–20, <https://doi.org/10.1016/j.jsg.2013.09.010>, 2014a.
- 450 Faria, S. H., Weikusat, I., and Azuma, N.: The Microstructure of Polar Ice. Part II: State of the Art, *Journal of Structural Geology*, 61, 21–49, <https://doi.org/10.1016/j.jsg.2013.11.003>, 2014b.
- Farinotti, D., Huss, M., Bauder, A., Funk, M., and Truffer, M.: A Method to Estimate the Ice Volume and Ice-Thickness Distribution of Alpine Glaciers, *Journal of Glaciology*, 55, 422–430, 2009.
- 455 Gagliardini, O., Zwinger, T., Gillet-Chaulet, F., Durand, G., Favier, L., de Fleurian, B., Greve, R., Malinen, M., Martín, C., Råback, P., Ruokolainen, J., Sacchetti, M., Schäfer, M., Seddik, H., and Thies, J.: Capabilities and Performance of Elmer/Ice, a New-Generation Ice Sheet Model, *Geoscientific Model Development*, 6, 1299–1318, <https://doi.org/10.5194/gmd-6-1299-2013>, 2013.
- Gillet-Chaulet, F., Gagliardini, O., Meyssonier, J., Montagnat, M., and Castelnau, O.: A User-Friendly Anisotropic Flow Law for Ice-Sheet Modeling, *Journal of Glaciology*, 51, 3–14, <https://doi.org/10.3189/172756505781829584>, 2005.
- 460 Glen, J. W.: The Creep of Polycrystalline Ice, *Proc. R. Soc. Lond. A*, 228, 519–538, <https://doi.org/10.1098/rspa.1955.0066>, 1955.
- Gow, A. J. and Meese, D.: Physical Properties, Crystalline Textures and c-Axis Fabrics of the Siple Dome (Antarctica) Ice Core, *Journal of Glaciology*, 53, 573–584, <https://doi.org/10.3189/002214307784409252>, 2007.
- Gow, A. J. and Williamson, T.: Rheological Implications of the Internal Structure and Crystal Fabrics of the West Antarctic Ice Sheet as Revealed by Deep Core Drilling at Byrd Station, *Geological Society of America Bulletin*, 87, 1665–1677, 1976.
- 465 Grab, M., Bauder, A., Ammann, F., Langhammer, L., Hellmann, S., Church, G. J., Schmid, L., Rabenstein, L., and Maurer, H. R.: Ice Volume Estimates of Swiss Glaciers Using Helicopter-Borne GPR — an Example from the Glacier de La Plaine Morte, in: 2018 17th International Conference on Ground Penetrating Radar (GPR), pp. 1–4, <https://doi.org/10.1109/ICGPR.2018.8441613>, 2018.
- Gräff, D., Walter, F., and Bauder, A.: Borehole Measurements and Basal Velocity of Rhonegletscher: Analysis of Borehole Measurements and Determination of the Basal Sliding Velocity of Rhonegletscher, in: 15th Swiss Geoscience Meeting (SGM 2017), p. P 9.10, ETH Zurich, Laboratory for Hydraulics, Hydrology and Glaciology, <https://doi.org/10.3929/ethz-b-000444720>, 2017.
- 470 Hambrey, M. J. and Milnes, A. G.: Structural Geology of an Alpine Glacier (Griesgletscher, Valais, Switzerland), *Eclogae Geologicae Helvetiae*, 70, 667–684, 1977.
- Hambrey, M. J., Milnes, A. G., and Siegenthaler, H.: Dynamics and Structure of Griesgletscher, Switzerland, *Journal of Glaciology*, 25, 215–228, <https://doi.org/10.3189/S0022143000010455>, 1980.
- 475 Hellmann, S., Kerch, J., Eichler, J., Jansen, D., Weikusat, I., Schwikowski, M., Bauder, A., and Maurer, H.: Crystal C-Axes Measurements (Fabric Analyser G50) of Ice Core Samples Collected from the Temperate Alpine Ice Core Rhone_2017, <https://doi.org/10.1594/PANGAEA.888518>, 2018.
- Herron, S. L. and Langway, C. C.: A Comparison of Ice Fabrics and Textures at Camp Century, Greenland and Byrd Station, Antarctica, *Annals of glaciology*, 3, 118–124, 1982.
- 480 Hooke, R. L.: Crystal Shape in Polar Glaciers and the Philosophy of Ice-Fabric Diagrams, *Journal of Glaciology*, 8, 324–326, <https://doi.org/10.3189/S002214300003135X>, 1969.
- Hooke, R. L.: Structure and Flow in the Margin of the Barnes Ice Cap, Baffin Island, N.W.T., Canada, *Journal of Glaciology*, 12, 423–438, <https://doi.org/10.3189/S0022143000031841>, 1973.

- Hooke, R. L. and Hudleston, P. J.: Origin of Foliation in Glaciers, *Journal of Glaciology*, 20, 285–299, 485 <https://doi.org/10.3189/S0022143000013848>, 1978.
- Hooke, R. L. and Hudleston, P. J.: Ice Fabrics in a Vertical Flow Plane, Barnes Ice Cap, Canada, *Journal of Glaciology*, 25, 195–214, <https://doi.org/10.3189/S0022143000010443>, 1980.
- Jacka, T. H. and Maccagnan, M.: Ice Crystallographic and Strain Rate Changes with Strain in Compression and Extension, *Cold Regions Science and Technology*, 8, 269–286, [https://doi.org/10.1016/0165-232X\(84\)90058-2](https://doi.org/10.1016/0165-232X(84)90058-2), 1984.
- 490 Jansen, D., Llorens Verde, M. G., Westhoff, J., Steinbach, F., Kipfstuhl, S., Bons, P. D., Griera, A., and Weikusat, I.: Small-Scale Disturbances in the Stratigraphy of the NEEM Ice Core: Observations and Numerical Model Simulations, *The Cryosphere*, 10, 359–370, <https://doi.org/10.5194/tc-10-359-2016> <<https://doi.org/10.5194/tc-10-359-2016>> , hdl:10013/epic.46883, 2016.
- Journaux, B., Chauve, T., Montagnat, M., Tommasi, A., Barou, F., Mainprice, D., and Gest, L.: Recrystallization Processes, Microstructure and Crystallographic Preferred Orientation Evolution in Polycrystalline Ice during High-Temperature Simple Shear, *The Cryosphere*, 13, 495 1495–1511, <https://doi.org/10.5194/tc-13-1495-2019>, 2019.
- Jouvet, G. and Funk, M.: Modelling the Trajectory of the Corpses of Mountaineers Who Disappeared in 1926 on Aletschgletscher, Switzerland, *Journal of Glaciology*, 60, 255–261, <https://doi.org/10.3189/2014JoG13J156>, 2014.
- Jouvet, G., Huss, M., Blatter, H., Picasso, M., and Rappaz, J.: Numerical Simulation of Rhonegletscher from 1874 to 2100, *Journal of Computational Physics*, 228, 6426–6439, <https://doi.org/10.1016/j.jcp.2009.05.033>, 2009.
- 500 Jouvet, G., Huss, M., Funk, M., and Blatter, H.: Modelling the Retreat of Grosser Aletschgletscher, Switzerland, in a Changing Climate, *Journal of Glaciology*, 57, 1033–1045, <https://doi.org/10.3189/002214311798843359>, 2011.
- Kamb, B.: Experimental Recrystallization of Ice under Stress, Washington DC American Geophysical Union Geophysical Monograph Series, 16, 211, <https://doi.org/10.1029/GM016p0211>, 1972.
- Kamb, W. B.: Ice Petrofabric Observations from Blue Glacier, Washington, in Relation to Theory and Experiment, *Journal of Geophysical Research*, 64, 1891–1909, <https://doi.org/10.1029/JZ064i011p01891>, 1959.
- 505 Krischke, A., Oechsner, U., and Kipfstuhl, S.: Rapid Microstructure Analysis of Polar Ice Cores, *Optik & Photonik*, 10, 32–35, <https://doi.org/10.1002/opph.201500016>, 2015.
- Kuiper, E.-J. N., de Bresser, J. H. P., Drury, M. R., Eichler, J., Pennock, G. M., and Weikusat, I.: Using a Composite Flow Law to Model Deformation in the NEEM Deep Ice Core, Greenland: Part 2 the Role of Grain Size and Premelting on Ice Deformation at High Homologous 510 Temperature, *The Cryosphere Discussions*, pp. 1–30, <https://doi.org/10.5194/tc-2018-275>, 2019.
- Llorens, M.-G., Griera, A., Bons, P. D., Lebensohn, R. A., Evans, L. A., Jansen, D., and Weikusat, I.: Full-Field Predictions of Ice Dynamic Recrystallisation under Simple Shear Conditions, *Earth and Planetary Science Letters*, 450, 233–242, <https://doi.org/10.1016/j.epsl.2016.06.045>, 2016.
- Llorens, M.-G., Griera, A., Steinbach, F., Bons, P. D., Gomez-Rivas, E., Jansen, D., Roessiger, J., Lebensohn, R. A., and Weikusat, I.: 515 Dynamic Recrystallization during Deformation of Polycrystalline Ice: Insights from Numerical Simulations, *Philosophical Transactions of the Royal Society A: Mathematical, Physical and Engineering Sciences*, 375, 20150346, <https://doi.org/10.1098/rsta.2015.0346>, 2017.
- Ma, Y., Gagliardini, O., Ritz, C., Gillet-Chaulet, F., Durand, G., and Montagnat, M.: Enhancement Factors for Grounded Ice and Ice Shelves Inferred from an Anisotropic Ice-Flow Model, *Journal of Glaciology*, 56, 805–812, <https://doi.org/10.3189/002214310794457209>, 2010.
- Maohuan, H., Ohtomo, M., and Wakahama, G.: Transition in Preferred Orientation of Polycrystalline Ice from Repeated Recrystallization, 520 *Annals of Glaciology*, 6, 263–264, <https://doi.org/10.3189/1985AoG6-1-263-264>, 1985.

- Matsuda, M. and Wakahama, G.: Crystallographic Structure of Polycrystalline Ice, *Journal of Glaciology*, 21, 607–620, <https://doi.org/10.3189/S0022143000033724>, 1978.
- Montagnat, M., Azuma, N., Dahl-Jensen, D., Eichler, J., Fujita, S., Gillet-Chaulet, F., Kipfstuhl, S., Samyn, D., Svensson, A., and Weikusat, I.: Fabric along the NEEM Ice Core, Greenland, and Its Comparison with GRIP and NGRIP Ice Cores, *The Cryosphere*, 8, 1129–1138, <https://doi.org/10.5194/tc-8-1129-2014>, 2014.
- 525 Monz, M. E., Hudleston, P. J., Prior, D. J., Michels, Z., Fan, S., Negrini, M., Langhorne, P. J., and Qi, C.: Electron Backscatter Diffraction (EBSD) Based Determination of Crystallographic Preferred Orientation (CPO) in Warm, Coarse-Grained Ice: A Case Study, Storglaciären, Sweden, *The Cryosphere Discussions*, pp. 1–24, <https://doi.org/10.5194/tc-2020-135>, 2020.
- Morgenthaler, J.: Modelling the Spatial Distribution of the Age of Ice on Rhonegletscher, Switzerland, Ph.D. thesis, ETH Zürich, Zurich, 530 2019.
- Patrick, B. A., Corvino, A. F., and Wilson, C. J. L.: Ice-Flow Measurements and Deformation at Marginal Shear Zones on Sørdsdal Glacier, Ingrid Christensen Coast, East Antarctica, *Annals of Glaciology*, 37, 60–68, <https://doi.org/10.3189/172756403781815933>, 2003.
- Peternell, M., Kohlmann, F., Wilson, C. J., Seiler, C., and Gleadow, A. J.: A New Approach to Crystallographic Orientation Measurement for Apatite Fission Track Analysis: Effects of Crystal Morphology and Implications for Automation, *Chemical Geology*, 265, 527–539, <https://doi.org/10.1016/j.chemgeo.2009.05.021>, 2009.
- 535 Petit, J. R., Jouzel, J., Raynaud, D., Barkov, N. I., Barnola, J.-M., Basile, I., Bender, M., Chappellaz, J., Davis, M., Delaygue, G., Delmotte, M., Kotlyakov, V. M., Legrand, M., Lipenkov, V. Y., Lorius, C., Pépin, L., Ritz, C., Saltzman, E., and Stievenard, M.: Climate and Atmospheric History of the Past 420,000 Years from the Vostok Ice Core, Antarctica, *Nature*, 399, 429–436, <https://doi.org/10.1038/20859>, 1999.
- 540 Pettit, E. C., Thorsteinsson, T., Jacobson, H. P., and Waddington, E. D.: The Role of Crystal Fabric in Flow near an Ice Divide, *Journal of Glaciology*, 53, 277–288, <https://doi.org/10.3189/172756507782202766>, 2007.
- Pettit, E. C., Waddington, E. D., Harrison, W. D., Thorsteinsson, T., Elsberg, D., Morack, J., and Zumberge, M. A.: The Crossover Stress, Anisotropy and the Ice Flow Law at Siple Dome, West Antarctica, *Journal of Glaciology*, 57, 39–52, <https://doi.org/10.3189/002214311795306619>, 2011.
- 545 Rigsby, G. P.: Crystal Fabric Studies on Emmons Glacier Mount Rainier, Washington, *The Journal of Geology*, 59, 590–598, 1951.
- Rigsby, G. P.: Crystal Orientation in Glacier and in Experimentally Deformed Ice, *Journal of Glaciology*, 3, 589–606, 1960.
- Robin, G. D. Q., Mitchell, G. F., and West, R. G.: Ice Cores and Climatic Change, *Philosophical Transactions of the Royal Society of London. B, Biological Sciences*, 280, 143–168, <https://doi.org/10.1098/rstb.1977.0103>, 1977.
- Russell-Head, D. S. and Budd, W. F.: Ice-Sheet Flow Properties Derived from Bore-Hole Shear Measurements Combined With Ice-Core 550 Studies, *Journal of Glaciology*, 24, 117–130, <https://doi.org/10.3189/S0022143000014684>, 1979.
- Schulson, E. M. and Duval, P.: Creep and Fracture of Ice, 2009.
- Schwikowski, M., Jenk, T. M., Stampfli, D., and Stampfli, F.: A New Thermal Drilling System for High-Altitude or Temperate Glaciers, *Annals of Glaciology*, 55, 131–136, <https://doi.org/10.3189/2014AoG68A024>, 2014.
- Steinbach, F., Bons, P. D., Griera, A., Jansen, D., Llorens Verde, M. G., Roessiger, J., and Weikusat, I.: Strain Localization and Dynamic 555 Recrystallization in the Ice–Air Aggregate: A Numerical Study, *The Cryosphere*, 10, 3071–3089, <https://doi.org/10.5194/tc-10-3071-2016>, 2016.

- Steinbach, F., Kuiper, E.-J. N., Eichler, J., Bons, P. D., Drury, M. R., Griera, A., Pennock, G. M., and Weikusat, I.: The Relevance of Grain Dissection for Grain Size Reduction in Polar Ice: Insights from Numerical Models and Ice Core Microstructure Analysis, *Frontiers in Earth Science*, 5, <https://doi.org/10.3389/feart.2017.00066>, 2017.
- 560 Thompson, L. G., Mosley-Thompson, E., Davis, M. E., Henderson, K. A., Brecher, H. H., Zagorodnov, V. S., Mashiotta, T. A., Lin, P.-N., Mikhalenko, V. N., Hardy, D. R., and Beer, J.: Kilimanjaro Ice Core Records: Evidence of Holocene Climate Change in Tropical Africa, *Science*, 298, 589–593, <https://doi.org/10.1126/science.1073198>, 2002.
- Thorsteinsson, T.: An Analytical Approach to Deformation of Anisotropic Ice-Crystal Aggregates, *Journal of Glaciology*, 47, 507–516, <https://doi.org/10.3189/172756501781832124>, 2001.
- 565 Thorsteinsson, T., Kipfstuhl, J., and Miller, H.: Textures and Fabrics in the GRIP Ice Core, *Journal of Geophysical Research: Oceans*, 102, 26 583–26 599, <https://doi.org/10.1029/97JC00161>, 1997.
- Thwaites, R. J., Wilson, C. J. L., and McCray, A. P.: Relationship Between Bore-Hole Closure and Crystal Fabrics in Antarctic Ice Core from Cape Folger, *Journal of Glaciology*, 30, 171–179, <https://doi.org/10.3189/S0022143000005906>, 1984.
- Tison, J.-L. and Hubbard, B.: Ice Crystallographic Evolution at a Temperate Glacier: Glacier de Tsanfleuron, Switzerland, *Geological Society, London, Special Publications*, 176, 23–38, 2000.
- 570 Vollmer, F. W.: C Program for Automatic Contouring of Spherical Orientation Data Using a Modified Kamb Method, *Computers & Geosciences*, 21, 31–49, 1995.
- Wallbrecher, E.: *Tektonische Und Gefügeanalytische Arbeitsweisen: Graphische, Rechnerische Und Statistische Verfahren*, Enke, Stuttgart, 1986.
- 575 Weikusat, I., Kipfstuhl, S., Azuma, N., Faria, S. H., and Miyamoto, A.: Deformation Microstructures in an Antarctic Ice Core (EDML) and in Experimentally Deformed Artificial Ice, *Low Temperature Science*, 68, 115–123, 2009a.
- Weikusat, I., Kipfstuhl, S., Faria, S. H., Azuma, N., and Miyamoto, A.: Subgrain Boundaries and Related Microstructural Features in EDML (Antarctica) Deep Ice Core, *Journal of Glaciology*, 55, 461–472, <https://doi.org/10.3189/002214309788816614>, 2009b.
- Weikusat, I., De Winter, D. A. M., Pennock, G. M., Hayles, M., Schneijdenberg, C., and Drury, M. R.: Cryogenic EBSD on Ice: Preserving 580 a Stable Surface in a Low Pressure SEM, *Journal of microscopy*, 242, 295–310, 2011a.
- Weikusat, I., Miyamoto, A., Faria, S. H., Kipfstuhl, S., Azuma, N., and Hondoh, T.: Subgrain Boundaries in Antarctic Ice Quantified by X-Ray Laue Diffraction, *Journal of Glaciology*, 57, 111–120, <https://doi.org/10.3189/002214311795306628>, 2011b.
- Weikusat, I., Jansen, D., Binder, T., Eichler, J., Faria, S. H., Wilhelms, F., Kipfstuhl, S., Sheldon, S., Miller, H., Dahl-Jensen, D., and Kleiner, T.: Physical Analysis of an Antarctic Ice Core—towards an Integration of Micro- and Macrodynamics of Polar Ice, *Philosophical Transactions of the Royal Society A: Mathematical, Physical and Engineering Sciences*, 375, 20150 347, <https://doi.org/10.1098/rsta.2015.0347>, 585 2017.
- Wilson, C. J., Russell-Head, D. S., and Sim, H. M.: The Application of an Automated Fabric Analyzer System to the Textural Evolution of Folded Ice Layers in Shear Zones, *Annals of Glaciology*, 37, 7–17, 2003.
- Wilson, C. J. L. and Peternell, M.: Evaluating Ice Fabrics Using Fabric Analyser Techniques in Sørdsal Glacier, East Antarctica, *Journal of 590 Glaciology*, 57, 881–894, <https://doi.org/10.3189/002214311798043744>, 2011.